MATERIALS SCIENCE

Spiral self-assembly of lamellar micelles into multi-shelled hollow nanospheres with unique chiral architecture

Liang Peng[1]†, Huarong Peng[1]†, Yu Liu[2]†, Xiao Wang[3], Chin-Te Hung[1], Zaiwang Zhao[1], Gang Chen[3], Wei Li[1]*, Liqiang Mai[2], Dongyuan Zhao[1]*

Functional carbon nanospheres are exceptionally useful, yet controllable synthesis of them with well-defined porosity and complex multi-shelled nanostructure remains challenging. Here, we report a lamellar micelle spiral self-assembly strategy to synthesize multi-shelled mesoporous carbon nanospheres with unique chirality. This synthesis features the introduction of shearing flow to drive the spiral self-assembly, which is different from conventional chiral templating methods. Furthermore, a continuous adjustment in the amphipathicity of surfactants can cause the packing parameter changes, namely, micellar structure transformations, resulting in diverse pore structures from single-porous, to radial orientated, to flower-like, and to multi-shelled configurations. The self-supported spiral architecture of these multi-shelled carbon nanospheres, in combination with their high surface area (~530 $m^2 g^{-1}$), abundant nitrogen content (~6.2 weight %), and plentiful mesopores (~2.5 nm), affords them excellent electrochemical performance for potassium-ion storage. This simple but powerful micelle-directed self-assembly strategy offers inspiration for future nanostructure design of functional materials.

INTRODUCTION

Carbon materials have attracted tremendous research attentions owing to their advantages of lightness, conductivity, high stability, controllable porosity, and tunable surface functionality (1–6). These unique structural characteristics enable them great potentials in various emerging fields such as adsorption (7), nanoreactor (8), catalysis (9), biomedicine (10, 11), energy conversion, and storage (12–14). Up to now, a series of functional carbon nanomaterials have successfully been synthesized with delicate control on the compositions (15–18), nanostructures (19–23), and morphologies (24–28). Among various structural designs, hollow carbon nanospheres are of great scientific and technological interests recently by virtue of their unique structural and functional characters (29–33). The built-in cavity and nanopores can not only offer more accessible active sites but also have buffering effect to sustain mechanical stress and volume deformation during the reaction, enabling hollow carbon nanospheres very suitable for object carrying and mass diffusion–limited applications.

Substantial efforts have been devoted to synthesize hollow carbon nanospheres in recent years, such as nanocasting (34), chemical etching (35), Pickering emulsion (36), self-assembly (37), and thermal decomposition (38). Notwithstanding the abovementioned advances in synthetic approaches, hollow carbon nanospheres reported so far usually have a relatively simple single-shelled configuration. Increasing the complexity of hollow structures, in terms of pore structure and cavity control, is highly desirable for both fundamental

studies and realization of various functionalities (39, 40). One particular area of interest is the constructing of multiple shells within hollow carbon nanospheres, namely, multi-shelled architectures, which will endow the structures with more heterogeneous interfaces, high surface-to-volume ratio, and short mass transport length and thus bring better physicochemical properties (41–45). However, until now, only few examples have been reported to synthesize multi-shelled carbon nanospheres (MCNs), and most of them suffered from uncontrollable size, small interlayer spacing (<5 nm), and nonuniform morphology. As a result, the loading capacity and buffering effect of cavities are severely weakened and thus limited in the range of applications. In addition, present achievements of MCNs are generally limited to simple ball-in-ball hollow architecture. Structurally self-supported effect of a continuously topological architecture, such as bio-inspired chiral geometry, would make materials more excellent in structural and mechanical stabilities (46, 47). Although these advantages are easy to imagine (48–52), the direct creation of uniform MCNs with well-defined porosity and unique chiral architecture still remains a big challenge.

Here, we report a lamellar micelle spiral self-assembly approach to synthesizing uniform mesoporous MCNs with unique chiral architecture. This synthesis involves the creation of a lamellar Pluronic P123/1,3,5-trimethylbenzene (TMB)/dopamine (DA) micelle system, which is driven by the shearing flow to direct the polymerization of precursors, and then intelligently self-assembled into multi-shelled nanospheres. The lamellar micelles can continuously grow spirally and clasp ring at end to form a stable full sphere as the multishells. Furthermore, continuous increase in hydrophobic/hydrophilic ratios of surfactant can induce the micelle structure gradually transformed from spherical to cylindrical and to lamellar one, bringing forth novel opportunity in constructing diverse nanostructures, such as single-porous, radially oriented, flower-like, and spiral MCNs. In particular, the resultant spiral MCNs show uniform particle size (~150 nm), high surface area (530 $m^2 g^{-1}$), large pore volume (1.0 $m^3 g^{-1}$), plentiful mesopores (~2.5 nm), abundant nitrogen content [6.2 weight % (wt %)], and unprecedented chiral

[1]Department of Chemistry, Laboratory of Advanced Materials, Shanghai Key Laboratory of Molecular Catalysis and Innovative Materials, iChEM and State Key Laboratory of Molecular Engineering of Polymers, Fudan University, Shanghai 200433, P. R. China. [2]State Key Laboratory of Advanced Technology for Materials Synthesis and Processing, Wuhan University of Technology, Wuhan 430070, P. R. China. [3]School of Physical Science and Technology, ShanghaiTech University, Shanghai 201210, P. R. China.
*Corresponding author. Email: weilichem@fudan.edu.cn (W.L.); dyzhao@fudan.edu.cn (D.Z.)
†These authors contributed equally to this work.

architecture. The spiral MCNs deliver superior rate capability (134 mA·hour g^{-1} at 5 A g^{-1}) and long cycling stability (112 mA·hour g^{-1} at 2 A g^{-1} after 500 cycles) when being used as an anode material for potassium ion batteries (KIBs). This simple yet powerful synthesis protocol opens up a multifunctional platform for construction of various sophisticated nanostructures for multiple applications.

RESULTS

Material synthesis and characterization

The MCNs can be prepared via a lamellar micelle spiral self-assembly strategy using Pluronic P123 as the soft template, TMB as the hydrophobic interaction mediation agent, and DA as the nitrogen and carbon source in the ethanol/water mixture (Fig. 1). First, the lamellar micelles composted of P123/TMB/DA were formed in the system by stirring at 300 rpm, which could be clearly observed from the reaction-evolution photos (fig. S1). Then, the composite micelles were dynamically assembled into the mesostructured polydopamine (PDA) nanospheres under the guidance of the shearing flow. Last, carbonization of the freeze-dried PDA nanospheres in N$_2$ atmosphere could lead to the formation of spiral MCNs with interesting chiral architecture.

The field-emission scanning electron microscopy (FESEM) images show that the as-made mesostructured PDA nanospheres are very uniform with an average particle size of ~180 nm (fig. S2, A and B). Transmission electron microscopy (TEM) images reveal that the as-made PDA nanospheres have a multi-shelled chiral hollow structure, and the average interlayer spacing between neighboring shells is measured to be ~20 nm (fig. S2, C and D). After the carbonization at 900°C under N$_2$ atmosphere, uniform mesoporous carbon nanospheres with a reduced particle size (~150 nm) can be obtained because of the thermolysis-induced structure shrinkage (Fig. 2, A and B). Thermogravimetric analysis result indicates that the carbon yield is as high as ~51 wt % (fig. S3). Impressively, the well-developed spiral structure can be well retained without collapse and deformation after the high-temperature calcination (Fig. 2C). Magnified TEM image clearly demonstrates that the multi-shelled architecture grows spirally from the particle center to the outer surface with a continuous geometry and clasp ring at end (Fig. 2D). Close observations reveal that the MCNs have both clockwise and anticlockwise spiral structures with an average shell thickness of ~13 nm (Fig. 2, E and F). The TEM tomography further confirms the formed three-dimensional spiral multi-shelled nanostructure (movie S1). The high-resolution TEM (HRTEM) image shows the typical amorphous phase of carbon framework with many structural defects (fig. S4A), which can be further confirmed by the corresponding selected-area electron diffraction pattern (fig. S4B). Element mappings of individually spiral MCN (Fig. 2G) show the uniform distribution of C, N, and O atoms in each carbon shell.

N$_2$ sorption isotherms of the spiral MCNs (Fig. 3A) show a type IV curve with a H$_4$-type hysteresis loop, indicating the lamellar mesopore structure of the materials (30, 53). The pore size distribution curve derived from the adsorption branch shows that the sample has bimodal mesopore sizes at ~2.5 and 16 nm based on the
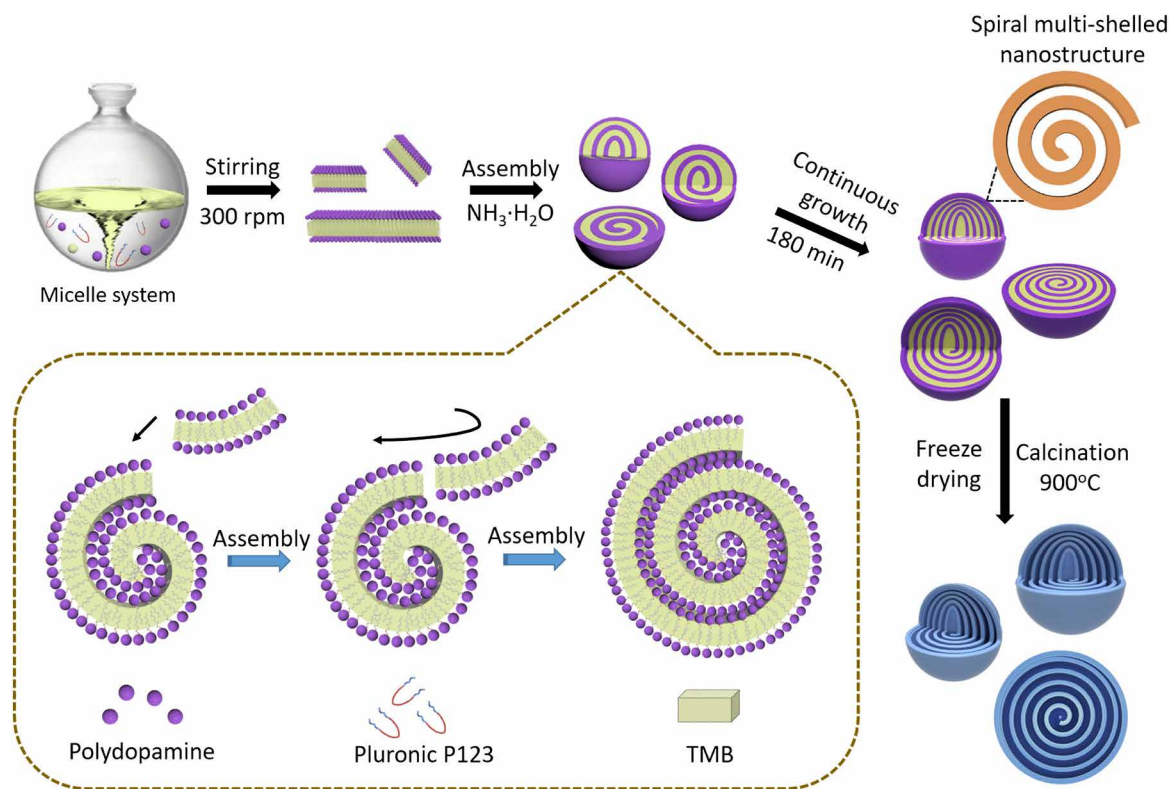
Fig. 1. Schematic representation of the formation process of the spiral MCNs First, the lamellar micelle system was formed by stirring the reactant at 300 rpm. Then, the lamellar micelles were dynamically assembled into the mesostructured PDA nanospheres under the guidance of the shearing flow. Last, carbonization of the freeze-dried PDA nanospheres in N$_2$ atmosphere could lead to the formation of spiral MCNs with interesting chiral architecture.
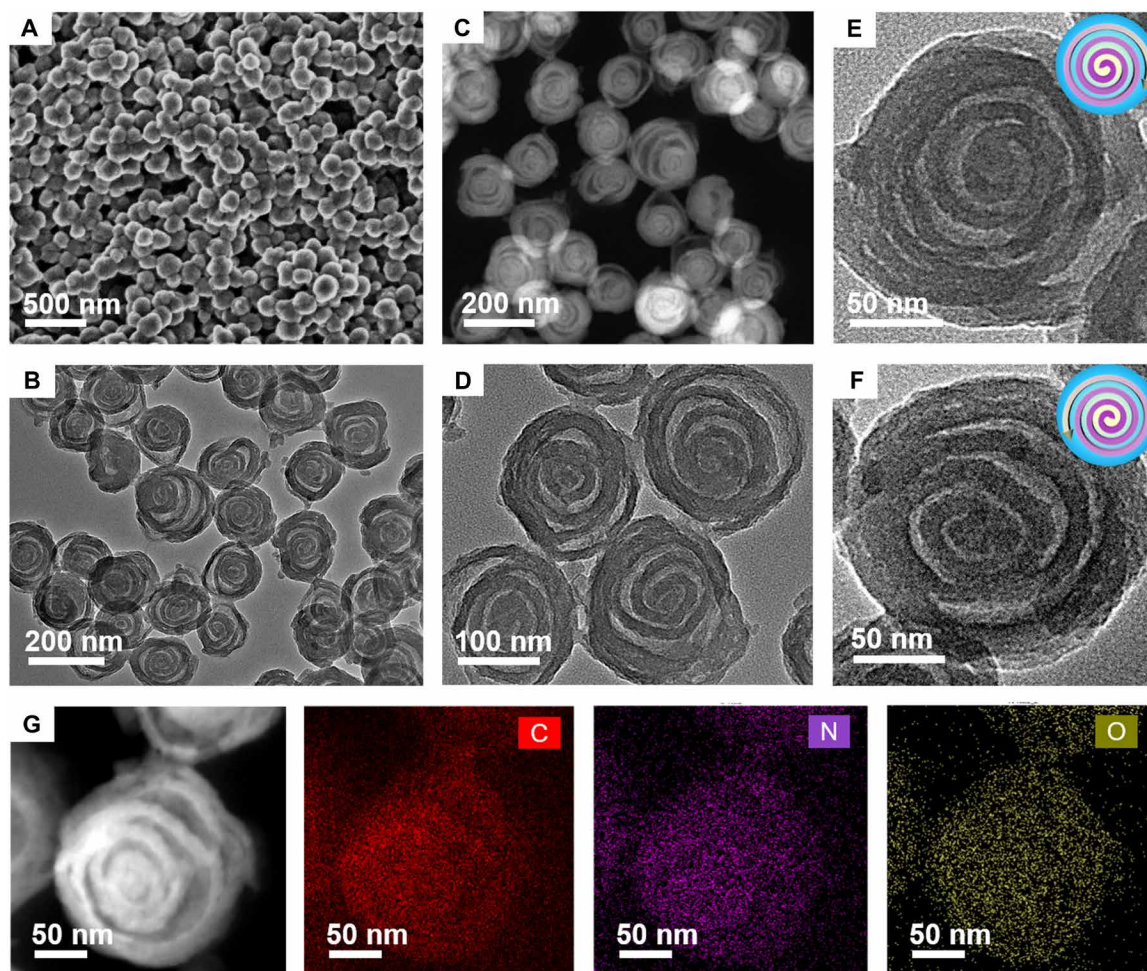
Fig. 2. Microstructure characterization of the spiral MCNs. (**A**) FESEM image, (**B** and **D**) TEM image, (**E** and **F**) magnified TEM images, and (**C** and **G**) scanning TEM and energy-dispersive x-ray element mapping images of the mesoporous MCNs with unique chiral architecture prepared by the lamellar micelle spiral self-assembly strategy.

Barrett-Joyner-Halenda model, which is in correspondence with the above TEM results (inset of Fig. 3A). In addition, the Brunauer-Emmett-Teller (BET) surface area and total pore volume are calculated to be ~530 m^2 g^{-1} and 1.0 cm^3 g^{-1}, respectively. Small-angle x-ray scattering (SAXS) pattern shows one resolved scattering peak (peak 5) with a high intensity at q value of ~0.23 nm^{-1}, which corresponds to the multi-shelled nanostructure with a d space of ~29 nm (Fig. 3B). This result is consistent with the sum of the carbon shell and interlayer spacing sizes. The other four weak scattering shoulders (peaks 1, 2, 3, and 4) at q values of about ~0.08, 0.11, 0.13 and 0.16 nm^{-1} are probably related to the diameter of the spiral MCN. The wide-angle x-ray diffraction pattern shows two diffraction peaks near 22.6° and 44.0°, which can be indexed to the (002) and (100) planes of hard carbon, respectively (fig. S5). The averaged D_{002} interlayer distance is calculated to be 3.97 Å based on the Bragg's law, which is much larger than that of the natural graphite (3.35 Å), suggesting modified amorphous feature. The Raman spectrum exhibits a high intensity ratio between the D band (defect-induced band, 1346 cm^{-1}) and the G band (crystalline graphite band, 1589 cm^{-1}), namely, I_D/I_G, revealing a low graphitization degree of carbon frameworks with rich defects (fig. S6). The x-ray photoelectron spectroscopy (XPS) survey shows that the spiral

MCNs are mainly composed of C, N, and O, with atomic percentages of 86.5, 6.2, and 7.3%, respectively (Fig. 3C). The high-resolution XPS spectrum of N 1s can be deconvoluted into four peaks as follows (Fig. 3D): pyridinic nitrogen (N-6, 398.4 eV), pyrrolic nitrogen (N-5, 399.6 eV), quaternary nitrogen (N-G, 400.7 eV), and oxidized nitrogen (N-O, 402.8 eV), indicating the favorable N-doped functionalities of the spiral MCNs.

The effect of solvent on the formation of the spiral MCNs was first investigated. When a few of ethanol present in the reaction system (20 volume %), irregular nanosheets consisted of interconnected small pieces could be formed (fig. S7A). By increasing the ethanol concentration to 50 volume %, the structure turned into multi-shelled PDA nanospheres with chiral architecture (fig. S7B). Further increasing the ethanol concentration to 80 volume %, the product was retained the regularity in spherical shape, but worm-like mesopores started to be observed (fig. S7C). Once the ethanol concentration increased up to 100 volume %, aggregated solid particles could appear without either well-defined mesopore or shape (fig. S7D). It is suggested that the presence of ethanol in the system helps to the formation of lamellar micelles, but excess ethanol can cause the micelle labile and even broken. Alternatively, by increasing the TMB/P123 mass ratio from 0.20 to 0.40, the structure of the products was
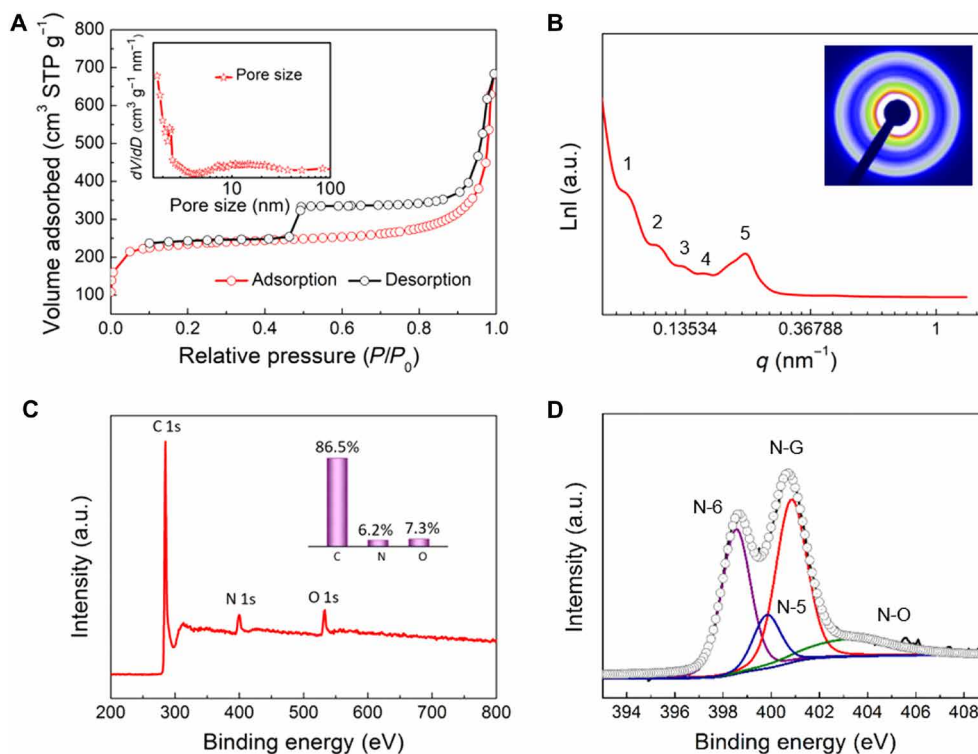
Fig. 3. Physicochemical characterization of the spiral MCNs. (**A**) N_2 sorption isotherms, (**B**) SAXS pattern, (**C**) XPS survey, and (**D**) high-resolution N 1s XPS spectrum of the mesoporous MCNs with unique chiral architecture prepared by the lamellar micelle spiral self-assembly strategy. Insets in (A) to (C) are the corresponding pore size distribution, two-dimensional SAXS image, and element weight percentages, respectively. a.u., arbitrary units.

varied from smooth solid nanospheres to triple-shelled one, and the shell thickness increased from about 20 to 50 nm (fig. S8, A and B). On further increasing the TMB/P123 mass ratio to 0.80, spiral multi-shelled nanospheres with a uniform shell thickness of ~16 nm and an interlayer spacing of ~20 nm could be produced (fig. S8C). When the TMB/P123 mass ratio reached to 1.20, the spherical morphology evolved into stacked nanobowls with opened nanostructure (fig. S8D). This variability in the product verifies that the TMB molecules not only can expand the lamellar micelle structure but also affect the lamellar micelle assembly behavior in the ethanol/water system.

Furthermore, the precursor amount and stirring rate effects on the morphology and mesostructure of MCNs were also investigated in the reaction system. When the DA amount was increased (0.25 to 0.50 g), the structure of the obtained products could be tuned from thin nanodisks to a mixture of single hollow and multi-shelled nanospheres (fig. S9, A and B). Further increasing the DA amount (0.75 g), the pure quintuple-shelled nanospheres with chiral architecture were fully developed (fig. S9C). By continuously increasing the DA amount (1.50 g), similar multi-shelled nanospheres but only double shells can be retained with a thick shell of ~40 nm (fig. S9D). It is suggested that the precursor amount has limited effect on the micellar structures but shows a great effect on the shell number and thickness of the products. On the other hand, in the absence of stirring, curved nanosheets with a thin thickness could be obtained (fig. S10A). Negligible change on the aspect of multi-shelled structure was demonstrated, while the stirring rate from 300 to 700 rpm was adopted (fig. S10, B and C). However, when a high stirring rate of 1000 rpm was used (fig. S10D), the multi-shelled structure was destroyed, and a mixture of nanosheets and broken

nanospheres were formed, which is mainly attributed to the tearing force caused by the turbulence in the reaction system. These results indicate that the driving force for the self-assembly of the multi-shelled nanostructure originates from agitation.

Moreover, the morphology and mesostructure of products can also be affected by the hydrophobic/hydrophilic ratio of the block co-polymer templates. Using of Pluronic F108 as a template, smooth carbon nanospheres were formed with single cavity in the center (Fig. 4, A to C). Changing the template from Pluronic F108 to F127, uniform radially oriented mesochannels could be observed in the carbon nanospheres (Fig. 4, D to F). By replacing the Pluronic F127 template by P105, the radial mesostructure was transformed into the dendritic mesoporous configuration consisting of crumpled nanosheets, such as flowers (Fig. 4, G to I). When using Pluronic P123 as a template, MCNs were generated with unique chiral architecture (Fig. 4, J to L). The BET surface areas of these resultant samples (denoted as MCN@x, where x represents the surfactant used) are calculated to be 135, 413, and 486 m^2 g^{-1}, and the corresponding total volumes are 0.42, 0.73, and 0.89 cm^3 g^{-1} for MCN@F108, MCN@F127, and MCN@P105, respectively (fig. S11). The pore sizes of them are centered at ~3, 7, and 12 nm, respectively (Fig. 4M). All of these data are summarized in table S1. This variability of mesostructure in the products confirms that the amphipathicity of block copolymer surfactants plays a critical role in the micellar morphology and structure control.

Electrochemical performance of the spiral MCNs as KIB anodes

The spiral MCNs were tested as anode materials for KIBs in the CR2032-type coin half cells. The electrolyte was a mixture of 0.8 M
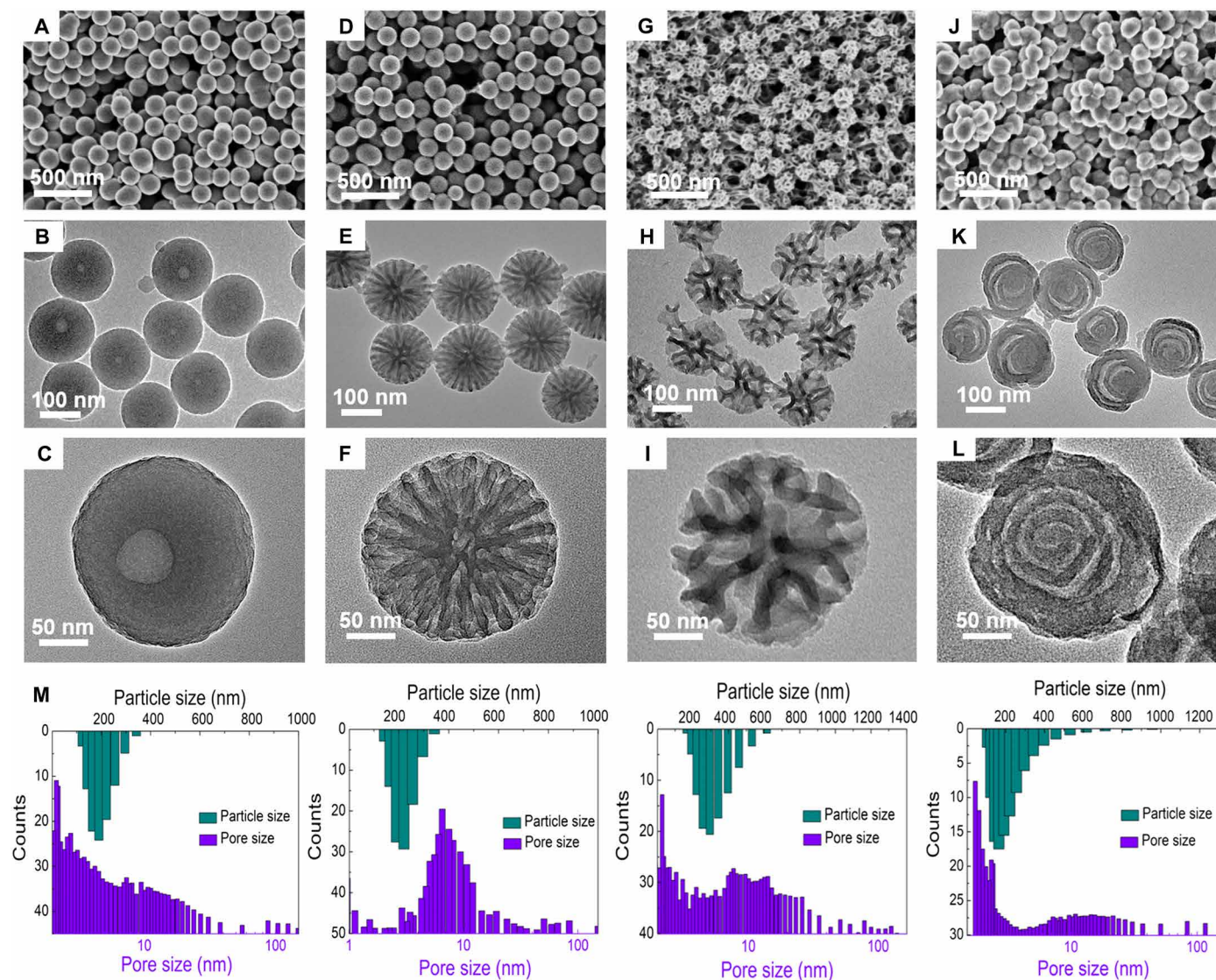
Fig. 4. The controllability and versatility of the synthetic method. FESEM and TEM images of the mesoporous carbon nanospheres prepared by adjusting the interfacial curvature of micelles through using different Pluronic triblock copolymers: (**A** to **C**) F108, (**D** to **F**) F127, (**G** to **I**) P105, and (**J** to **L**) P123. (**M**) The corresponding distribution histograms of the particle diameters and pore sizes.

KPF_6 in diethyl carbonate and ethylene carbonate (v/v, 1:1). The electrochemical performance was first evaluated by cyclic voltammetry (CV) in the voltage scope of 0.01 to 3.0 V (versus K/K^+) (Fig. 5A). During the initial cathodic scan, a broad reduction peak is located at ~0.85 V and disappears in the following cycles, as mainly due to the irreversible reactions and the formation of the solid electrolyte interphase (SEI) layer on the surface of an electrode (*54*). A pair of redox peaks at ~0.1 and 0.5 V is ascribed to the intercalation/deintercalation of K ions in the porous carbon framework. The nearly overlap of the subsequent CV cycles indicates the great electrochemical reversibility after the first cycle. The galvanostatic charge/discharge curves display a plateau at ~0.5 V and followed by a slope down to 0.01 V, demonstrating the surface-driven dominated potassium storage behavior (Fig. 5B). The specific discharge capacity in the first cycle is 653 mA·hour g^{-1} with the charge capacity as high as 370 mA·hour g^{-1}, corresponding to an initial coulombic efficiency

(ICE) of 52%. The relatively low ICE should be attributed to the porous structure, which consumes a large amount of electrolytes for SEI layer formation. A specific capacity of 294 mA·hour g^{-1} is maintained after 100 cycles at a current density of 0.1 A g^{-1}, indicating the excellent cycling stability (Fig. 5C), which is much superior to the solid carbon nanospheres (fig. S12). The TEM image and N_2 sorption isotherms analyses show that the multi-shelled mesoporous structure can be well retained even after a long-term cycle (fig. S13).

These spiral multi-shelled advantages became more prominent at higher current densities. The specific reversible capacities are measured to be 275, 226, 198, and 174 mA·hour g^{-1} at the current densities of 0.2, 0.5, 1.0, and 2.0 A g^{-1}, respectively (Fig. 5D). Impressively, a decent capacity of 134 mA·hour g^{-1} can still be retained with further increasing the current density to 5.0 A g^{-1}. When the current rate is switched back to 0.2 A g^{-1}, a reversible capacity of 241 mA·hour g^{-1} can be recovered, demonstrating the excellent rate
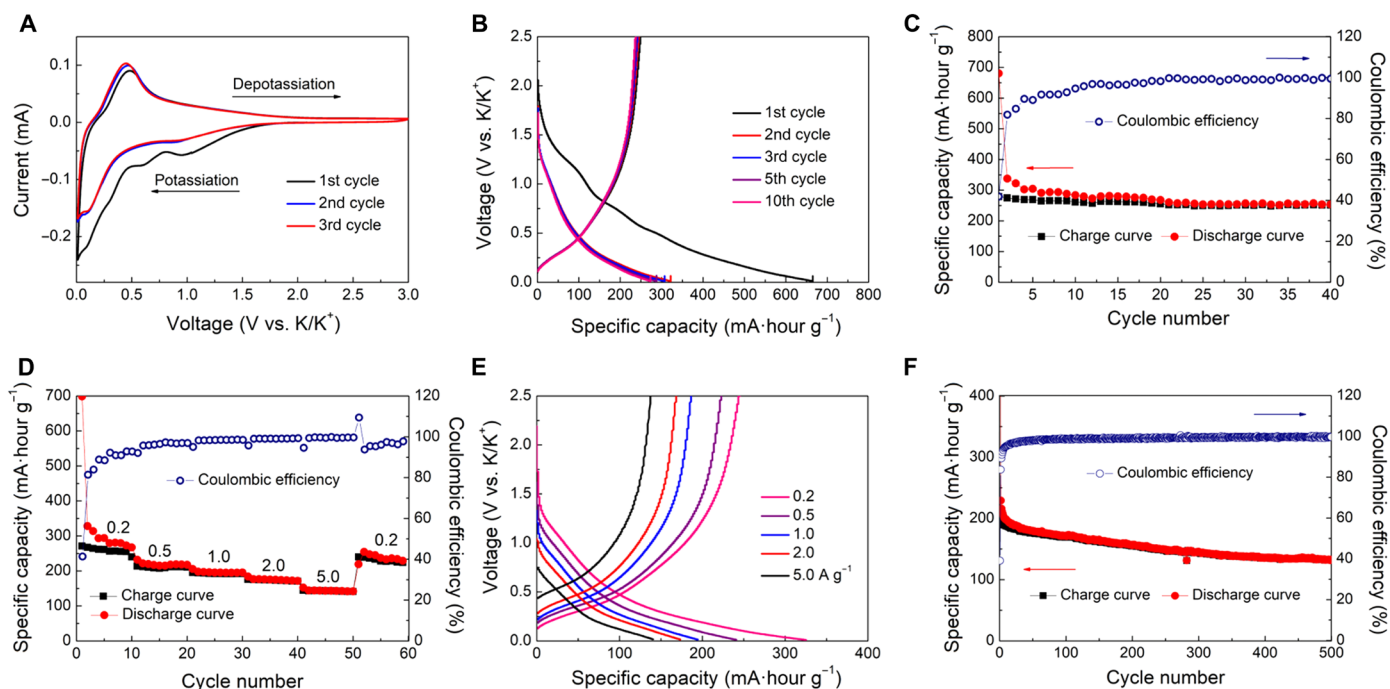
Fig. 5. Electrochemical performances of the spiral MCNs as anodes for KIBs. (**A**) CV curves at a scan rate of 0.1 mV s^{-1}, (**B**) charge/discharge curves at a current density of 0.1 A g^{-1}, (**C**) reversible capacity tests at a current density of 0.1 A g^{-1}, (**D** and **E**) rate capability tests from 0.2 to 5.0 A g^{-1}, and (**F**) cycling stability at 2.0 A g^{-1} for 500 cycles.

performance (Fig. 5E). After being tested at 2.0 A g^{-1} over 500 cycles, the spiral MCN electrode retained a stable capacity of 112 mA·hour g^{-1} with slight capacity decay of ~0.03% per cycle (Fig. 5F). Meanwhile, its CE value is nearly 100% after first few cycles. The electrochemical impedance spectrum of the spiral MCN electrode shows a small semicircle diameter and high line slope in the moderate and low frequency regions, respectively, indicating excellent charge and ion transfer kinetics (fig. S14). Ex situ Raman spectra show that the I_D/I_G ratios are gradually decreased from 1.18 to 1.01 and then backed to 1.17 during the discharge/charge process, suggesting that the potassium storage process is highly reversible (fig. S15). Corresponding HRTEM images further confirm that the carbon frameworks are integrated and undergone reversible expansion/contraction during cycling, thus enabling stable insertion/extraction of K ion (fig. S16). In addition, when the spiral MCNs used as the anode materials for lithium ion batteries, the reversible capacities of 143 mA·hour g^{-1} can be remained after 1000 cycles at 5.0 A g^{-1}, indicating wide application potentials of the spiral MCNs (fig. S17). Compared to the works from the recent literature (table S2), the spiral MCN shows an attractive rate capability and impressive cycling performance.

To gain more insights into the electrochemical behavior of the spiral MCN electrode, we conducted the kinetics and quantitative analysis based on the CV tests at varying scan rates from 0.2 to 2.0 mV s^{-1}. The redox peaks keep their original shapes and slightly expand to cover higher voltages along with the increasing scan rates, indicating a surface-dominated K ion storage feature (Fig. 6A). Even at a high scan rate of 2.0 mV s^{-1}, it also shows well-defined redox peaks, demonstrating very small polarization. Here, the relationship between the peak current (*i*) and the scan rate (*v*) obeys a power law, which can be described in Eqs. 1 and 2

$$i = av^b \qquad (1)$$

$$\log(i) = b\log(v) + \log(a) \qquad (2)$$

where *i* represents the peak current (in milliamperes), *v* is the scan rate (in millivolts per second), and *a* and *b* are the adjustable constants. The *b* value is equal to the slope by fitting the $\log(i)$-$\log(v)$ plots. In particular, the *b* value close to 0.5 indicates a diffusion-dominated process, whereas 1.0 signifies the capacitive-controlled process. In our case, the curve shows a well-defined linear relationship, and the *b* values for cathodic (peak 1) and anodic peaks (peaks 2 and 3) are calculated to be 0.92, 0.99, and 0.94, respectively, suggesting the dominant fast kinetics of capacitive-controlled behavior (Fig. 6B). Furthermore, the capacitive charge contribution can be further distinguished in Eq. 3

$$i(V) = k_1 v + k_2 v^{1/2} \qquad (3)$$

in which both k_1 and k_2 are constants, and $k_1 v$ represents the surface capacitive fraction while $k_2 v^{1/2}$ corresponds to the diffusion-controlled process. On the basis of the quantification, about 74.6% of the total charge is capacitive at a low scan rate of 1.0 mV s^{-1}, indicating the capacitive dominated behavior (Fig. 6C). When being tested at other scan rates of 0.2, 0.4, 0.6, 0.8, 1.2, and 1.4, the capacitive contribution ratios are 61.8, 64.8, 68.8, 71.3, 75.3, and 77.4%, respectively (Fig. 6D). The results reveal that the capacitive contribution ratio gradually increases with the increase in scan rate and lastly reaches a maximum value of 83.7% at 2.0 mV s^{-1}, further demonstrating the advantages of the multi-shelled spiral structure.
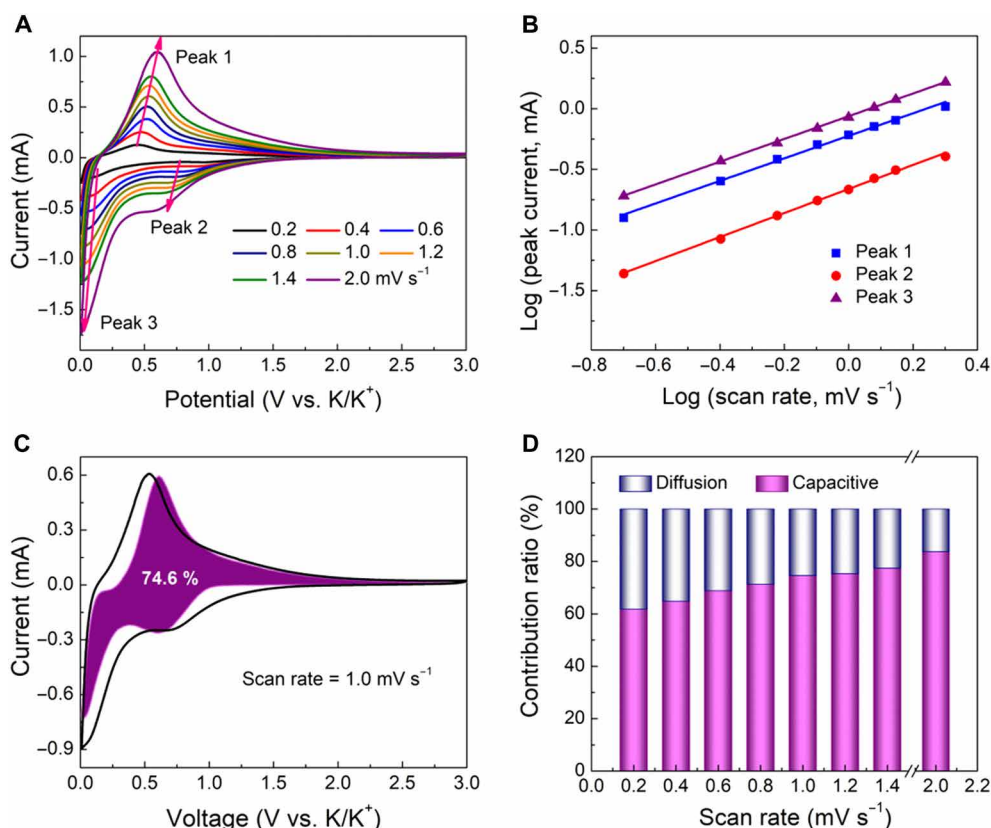
Fig. 6. Kinetics analyses of the potassium storage behaviors for the chiral MCN electrode. (**A**) CV curves at various scan rates from 0.2 to 2.0 mV s^{-1}, (**B**) determination of *b* values using the relationship peak current and scan rate, (**C**) separation of the capacitive and diffusion currents at a scan rate of 1.0 mV s^{-1}, and (**D**) contribution ratio of the capacitive and diffusion-controlled charge versus different scan rates.

DISCUSSION

In general, the direct creation of multi-shelled carbon structures through block copolymer self-assembly depends on the competition between bending energy and layer-to-layer interactions. Rational control of the micelle structure with the introduction of appropriate mediation agent might allow finely balancing of the abovementioned competition. In conventional synthesis, the micellar structure can be guided by the surfactant packing parameter (*P*), which is defined in Eq. 4

$$P = \frac{v_0}{al_0} \qquad (4)$$

where v_0 and l_0 are the volume and length of the hydrophobic block, respectively, and *a* is the polar head surface area. For a certain surfactant, *P* is mainly determined by the hydrophobic/hydrophilic ratio, namely, V_H/V_L value [where V_H and V_L are the hydrophobic [poly(propylene oxide)] and hydrophilic [poly (ethylene oxide)] volume fractions, respectively]. Thus, continuous increase in V_H/V_L can induce a gradual increase in *P* accompanied with micellar structure transformation from spherical to lamellar, enabling the possibility to continuously tune pore structures. However, when the absence of PEO or PPO blocks in block copolymer surfactants ($V_H/V_L = \infty/0$), complete micelle cannot be formed, leading to the formation of non-porous aggregated particles (fig. S18). A low of V_H/V_L value (0.27, F108) can endow the surfactant with strongly hydrophilic PEO blocks; thus, only unfolding Pluronic F108 can be formed in the system.

However, the F108 molecules can direct the polymerization of DA and self-assembly around the TMB droplets, resulting in the formation of smooth nanospheres with a single cavity in the center (Fig. 7A). Increasing the V_H/V_L value (~0.46, $P \leq {}^1/_3$) enables the formation of stable spherical F127/TMB/DA micelles with high interfacial curvature and swelled size (Fig. 7B). Along with the shearing flow from the agitation, the large spherical micelles experience a touching, deforming, and fusing process in the radial direction to generate radially oriented mesoporous nanospheres. By continuously increasing the V_H/V_L value (~1.06, ${}^1/_3 \leq P \leq {}^1/_2$) can induce interfacial curvature decrease; thus, the cylindrical P105/TMB/DA composite micelles appear and assemble with DA molecules to form the flower-like nanospheres with a macro-/mesoporous architecture (Fig. 7C). Further increasing the V_H/V_L value (~2.43, ${}^1/_2 \leq P \leq 1$) can cause the micelle structure transformed into sandwich-like lamellar P123/TMB/DA one with lower interfacial curvature (Fig. 7D). In the lamellar P123/TMB/DA micelles, hydrophobic TMB molecules in the center can interact with the PPO segments of Pluronic P123 at both ends through van der Waals force, endowing the composite micelles with good stability and expanded size. Alternatively, DA molecules can polymerize quickly under alkaline condition, and the resultant PDA frameworks can conversely stabilize the multi-shelled nanostructure during the self-assembly process via π-π bonding. As agitation is adopted, the shearing flow drives the lamellar micelles to layer-by-layer dynamical self-assembly around the spiral axis, resulting in the spiral multi-shelled nanostructure from the inside out (fig. S19 and movie S2).
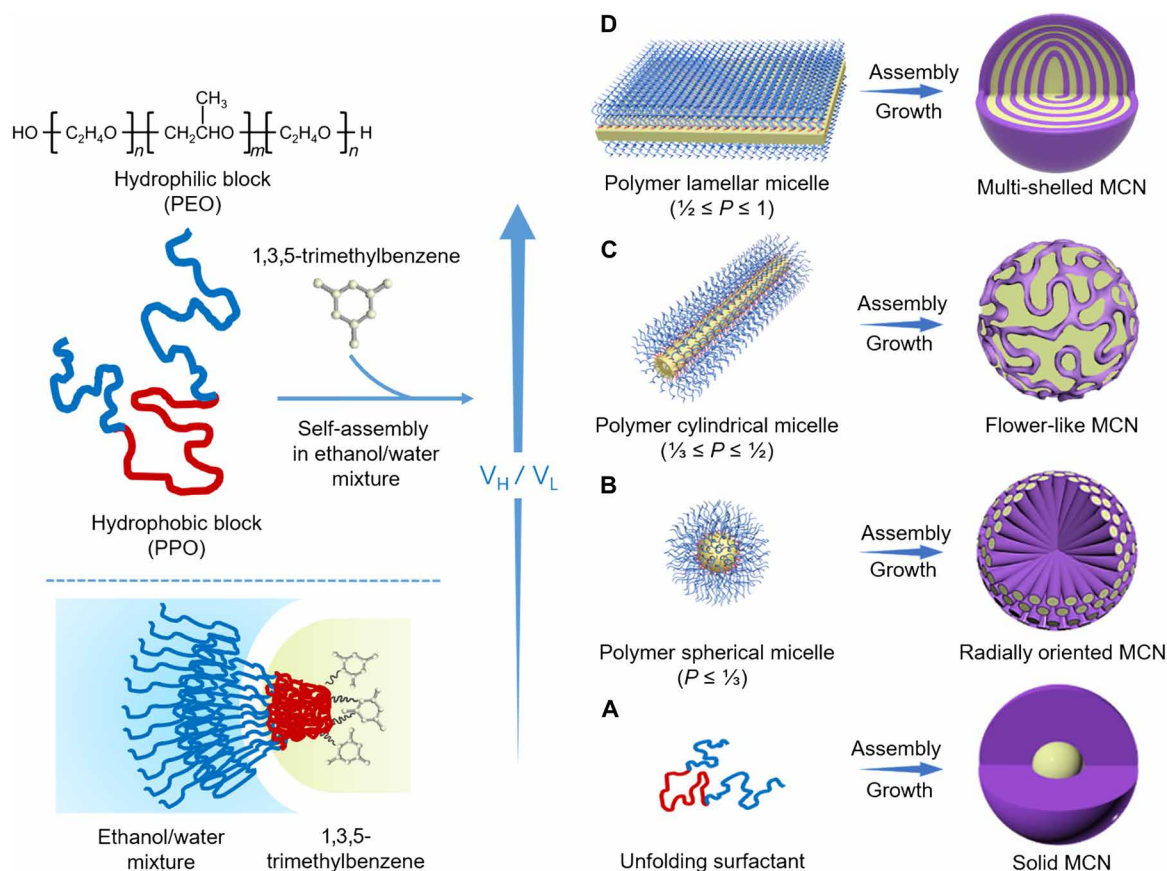
Fig. 7. Schematic illustration of the formation mechanism for the mesoporous carbon nanospheres with diverse architectures. A series of mesoporous carbon nanospheres were prepared using various triblock copolymers with different hydrophobic/hydrophilic ratios as templates: (**A**) F108, (**B**) F127, (**C**) P105, and (**D**) P123.

Therefore, the multi-shelled PDA nanospheres can be realized owing to the formation of a delicately dynamic balance between bending energy and layer-to-layer interactions during the self-assembly process (*55*). Fourier transform infrared spectroscopy spectra show that the catechol and amino groups of DA were oxidized to quinone and secondary amine groups during the synthesis process, resulting in the PDA frameworks (fig. S20). The solid-state ^{13}C nuclear magnetic resonance spectrum further reveals that the PDA frameworks are primarily consisted of 5,6-dihydroxyindoline and 5,6-indoleindoline units (fig. S21). The circular dichroism spectrum assisted with ultraviolet-visible spectrum shows a clear peak centered at 280 nm, which ascribes to the adsorption signal of colloidal PDA, confirming the formation of chiral nanostructures (fig. S22). Only positive signals can be observed under both clockwise and anticlockwise stirrings, indicating that the spiral nanostructure is independent of the stirring direction. This is because the formed multi-shelled nanostructure is a scroll-like nanosphere with a central axis. The tilting experiments further verify the spiral multi-shelled nanostructure from different viewing angles (fig. S23). In addition, a MATLAB program was developed, which can well simulate the spiral multi-shelled nanostructure (fig. S24), further demonstrating that the proposed spiral nanostructure is geometrically possible.

The superior rate capability and excellent cycle stability are mainly attributed to the unique spiral nanostructures and chemical properties of the spiral MCNs. The nanoscale particle size and hollow structure enable the shortened K ion diffusion lengths and offer plentiful storage active sites for K ion storage. Meanwhile, the spiral multi-shelled structure not only facilitates the continuously transfer of charges and ions to the whole carbon matrix but also contributes to buffer the mechanical stress/strain and volume change caused by the K ion insertion/extraction, especially in the cases of large current density and long cycling process. Besides, the micro-/mesopores existed in the thin shells and large interlayer spacings are highly permeable for comprehensive electrode/electrolyte contact externally and internally. In addition, the high content of N doping can bring more surface defects and edges of graphene layers that can improve K ion adsorption and therefore results in fast kinetics and high capacities.

In summary, uniform MCNs with well-defined porosity and unique chiral architecture have been fabricated via a lamellar micelle spiral self-assembly approach. This approach features the introduction of shearing flow to drive the lamellar micelles continuously self-assembled into stably spiral multi-shelled nanospheres with clasp ring at end. Furthermore, the micellar structure in this synthesis can be on-demand and systematically tuned by manipulating the hydrophobic/hydrophilic ratio of surfactants, which results in the controllable mesostructures from single-porous, to radially oriented, to flower-like, and to multi-shelled nanospheres. Impressively, the resultant spiral MCNs show small particle size (~150 nm), large

surface area (~530 m^2 g^{-1}), high pore volume (~1.0 m^3 g^{-1}), abundant N content (~6.2 wt %), thin shell thickness (~13 nm), and unprecedented chiral architecture. As a result, the MCNs deliver excellent rate capability (134 mA·hour g^{-1} at 5 A g^{-1}) and long-term cyclic stability (112 mA·hour g^{-1} at 2 A g^{-1} after 500 cycles) for KIBs. We believe that this work not only presents a multifunctional platform toward synthesis of novel nanostructures for advanced applications but also provides new and foundational knowledges on micelle-directed self-assembly and chemistry.

MATERIALS AND METHODS

The spiral multi-shelled mesoporous carbon nanospheres were fabricated by a lamellar micelle spiral self-assembly approach (see Supplementary Materials and Methods for detailed synthetic process). Briefly, Pluronic P123 (PEO$_{20}$PPO$_{70}$PEO$_{20}$), TMB (C$_9$H$_{12}$), and DA hydrochloride (C$_8$H$_{11}$NO$_2$·HCl) were stirred in a water/ethanol mixture with a designed mass ratio. Then, ammonium hydroxide was added to induce the polymerization of the DA precursor and assembly into the mesostructured PDA nanospheres. Last, carbonization of the freeze-dried polymer nanospheres in N$_2$ atmosphere could lead to the formation of spiral MCNs with interesting chiral architecture.

SUPPLEMENTARY MATERIALS

Supplementary material for this article is available at https://science.org/doi/10.1126/sciadv.abi7403

REFERENCES AND NOTES

1. Y. Yang, X. Yang, L. Liang, Y. Gao, H. Cheng, X. Li, X. Zou, R. Ma, Q. Yuan, X. Duan, Large-area graphene-nanomesh/carbon-nanotube hybrid membranes for ionic and molecular nanofiltration. *Science* 364, 1057–1062 (2019).
2. C. H. J. Evers, J. A. Luiken, P. G. Bolhuis, W. K. Kegel, Self-assembly of microcapsules via colloidal bond hybridization and anisotropy. *Nature* 534, 364–368 (2016).
3. W. Li, J. Liu, D. Y. Zhao, Mesoporous materials for energy conversion and storage devices. *Nat. Rev. Mater.* 1, 16023 (2016).
4. J. Liu, N. P. Wickramaratne, S. Z. Qiao, M. Jaroniec, Molecular-based design and emerging applications of nanoporous carbon spheres. *Nat. Mater.* 14, 763–774 (2015).
5. J. Knossalla, D. Jalalpoor, F. Schüth, Hands-on guide to the synthesis of mesoporous hollow graphitic spheres and core-shell materials. *Chem. Mater.* 29, 7062–7072 (2017).
6. J. Zhang, Z. Xia, L. Dai, Carbon-based electrocatalysts for advanced energy conversion and storage. *Sci. Adv.* 1, e1500564 (2015).
7. N. P. Wickramaratne, J. Xu, M. Wang, L. Zhu, L. Dai, M. Jaroniec, Nitrogen enriched porous carbon spheres: Attractive materials for supercapacitor electrodes and CO$_2$ adsorption. *Chem. Mater.* 26, 2820–2828 (2014).
8. H. Tian, J. Liang, J. Liu, Nanoengineering carbon spheres as nanoreactors for sustainable energy applications. *Adv. Mater.* 31, 1903886 (2019).
9. H. Zhang, P. An, W. Zhou, B. Y. Guan, P. Zhang, J. Dong, X. W. D. Lou, Dynamic traction of lattice-confined platinum atoms into mesoporous carbon matrix for hydrogen evolution reaction. *Sci. Adv.* 4, eaao6657 (2018).
10. F. Yuan, S. Li, Z. Fan, X. Meng, L. Fan, S. Yang, Shining carbon dots: Synthesis and biomedical and optoelectronic applications. *Nano Today* 11, 565–586 (2016).
11. M. S. Kim, J. Lee, H. S. Kim, A. Cho, K. H. Shim, T. N. Le, S. S. A. An, J. W. Han, M. I. Kim, J. Lee, Heme cofactor-resembling Fe-N single site embedded graphene as nanozymes to selectively detect H$_2$O$_2$ with high sensitivity. *Adv. Funct. Mater.* 30, 1905410 (2020).
12. W. Chen, G. Li, A. Pei, Y. Li, L. Liao, H. Wang, J. Wan, Z. Liang, G. Chen, H. Zhang, J. Wang, Y. Cui, A manganese-hydrogen battery with potential for grid-scale energy storage. *Nat. Energy* 3, 428–435 (2018).
13. J. L. Xia, J. Yan, L. P. Guo, X. L. Dong, A. H. Lu, Hard carbon nanosheets with uniform ultramicropores and accessible functional groups showing high realistic capacity and superior rate performance for sodium-ion storage. *Adv. Mater.* 32, 2000447 (2020).
14. T. Lin, I.-W. Chen, F. Liu, C. Yang, H. Bi, F. Xu, F. Huang, Nitrogen-doped mesoporous carbon of extraordinary capacitance for electrochemical energy storage. *Science* 350, 1508–1513 (2015).
15. F. Han, R. Wang, B. Chen, Y. Feng, H. Liu, S. Wang, D. Su, H. Zhang, H. Chen, Precise dimerization of hollow fullerene compartments. *J. Am. Chem. Soc.* 142, 15396–15402 (2020).
16. F. Han, R. Wang, Y. Feng, S. Wang, L. Liu, X. Li, Y. Han, H. Chen, On demand synthesis of hollow fullerene nanostructures. *Nat. Commun.* 10, 1548 (2019).
17. J. Liang, Y. Jiao, M. Jaroniec, S. Z. Qiao, Sulfur and nitrogen dual-doped mesoporous graphene electrocatalyst for oxygen reduction with synergistically enhanced performance. *Angew. Chem. Int. Ed.* 51, 11496–11500 (2012).
18. H. Peng, B. Yao, X. Wei, T. Liu, T. Kou, P. Xiao, Y. Zhang, Y. Li, Pore and heteroatom engineered carbon foams for supercapacitors. *Adv. Energy Mater.* 9, 1803665 (2019).
19. L. Peng, C.-T. Hung, S. Wang, X. Zhang, X. Zhu, Z. Zhao, C. Wang, Y. Tang, W. Li, D. Zhao, Versatile nanoemulsion assembly approach to synthesize functional mesoporous carbon nanospheres with tunable pore sizes and architectures. *J. Am. Chem. Soc.* 141, 7073–7080 (2019).
20. B. Y. Guan, S. L. Zhang, X. W. Lou, Realization of walnut-shaped particles with macro-/mesoporous open channels through pore architecture manipulation and their use in electrocatalytic oxygen reduction. *Angew. Chem. Int. Ed.* 57, 6176–6180 (2018).
21. G. Zhan, H. C. Zeng, A synthetic protocol for preparation of binary multi-shelled hollow spheres and their enhanced oxidation application. *Chem. Mater.* 29, 10104–10112 (2017).
22. F. Xie, L. Zhang, C. Ye, M. Jaroniec, S. Z. Qiao, The application of hollow structured anodes for sodium-ion batteries: From simple to complex systems. *Adv. Mater.* 31, 1800492 (2019).
23. J. Tang, J. Liu, C. Li, Y. Li, M. O. Tade, S. Dai, Y. Yamauchi, Synthesis of nitrogen-doped mesoporous carbon spheres with extra-large pores through assembly of diblock copolymer micelles. *Angew. Chem. Int. Ed.* 54, 588–593 (2015).
24. J. Tang, Y. Yamauchi, MOF morphologies in control. *Nat. Chem.* 8, 638–639 (2016).
25. S. Kim, J. Hwang, J. Lee, J. Lee, Polymer blend directed anisotropic self-assembly toward mesoporous inorganic bowls and nanosheets. *Sci. Adv.* 6, eabb3814 (2020).
26. S. Kim, M. Ju, J. Lee, J. Hwang, J. W. Lee, Polymer interfacial self-assembly guided two-dimensional engineering of hierarchically porous carbon nanosheets. *J. Am. Chem. Soc.* 142, 9250–9257 (2020).
27. F. Pei, L. Lin, A. Fu, S. Mo, D. Ou, X. Fang, N. Zheng, A two-dimensional porous carbon-modified separator for high-energy-density Li-S batteries. *Joule* 2, 323–336 (2018).
28. Z. Zhou, T. Liu, A. U. Khan, G. L. Liu, Block copolymer-based porous carbon fibers. *Sci. Adv.* 5, eaau6852 (2019).
29. L. Peng, H. Peng, C.-T. Hung, D. Guo, L. Duan, B. Ma, L. Liu, W. Li, D. Zhao, Programmable synthesis of radially gradient-structured mesoporous carbon nanospheres with tunable core-shell architectures. *Chem* 7, 1020–1032 (2021).
30. Q. Sun, B. He, X.-Q. Zhang, A.-H. Lu, Engineering of hollow core-shell interlinked carbon spheres for highly stable lithium-sulfur batteries. *ACS Nano* 9, 8504–8513 (2015).
31. L. Wang, Q. Sun, X. Wang, T. Wen, J.-J. Yin, P. Wang, R. Bai, X.-Q. Zhang, L.-H. Zhang, A.-H. Lu, C. Chen, Using hollow carbon nanospheres as a light-induced free radical generator to overcome chemotherapy resistance. *J. Am. Chem. Soc.* 137, 1947–1955 (2015).
32. Y. Cao, L. Xiao, M. L. Sushko, W. Wang, B. Schwenzer, J. Xiao, Z. Nie, L. V. Saraf, Z. Yang, J. Liu, Sodium ion insertion in hollow carbon nanowires for battery applications. *Nano Lett.* 12, 3783–3787 (2012).
33. F. Pei, T. An, J. Zang, X. Zhao, X. Fang, M. Zheng, Q. Dong, N. Zheng, From Hollow carbon spheres to N-doped hollow porous carbon bowls: Rational design of hollow carbon host for Li-S batteries. *Adv. Energy Mater.* 6, 1502539 (2016).
34. S. Yang, X. Feng, L. Zhi, Q. Cao, J. Maier, K. Müellen, Nanographene-constructed hollow carbon spheres and their favorable electroactivity with respect to lithium storage. *Adv. Mater.* 22, 838–842 (2010).
35. H. Zhang, O. Noonan, X. Huang, Y. Yang, C. Xu, L. Zhou, C. Z. Yu, Surfactant-free assembly of mesoporous carbon hollow spheres with large tunable pore sizes. *ACS Nano* 10, 4579–4586 (2016).
36. M. Li, Y. Zhang, X. Wang, W. Ahn, G. Jiang, K. Feng, G. Lui, Z. Chen, Gas pickering emulsion templated hollow carbon for high rate performance lithium sulfur batteries. *Adv. Funct. Mater.* 26, 8408–8417 (2016).
37. D. Gu, H. Bongard, Y. Deng, D. Feng, Z. Wu, Y. Fang, J. Mao, B. Tu, F. Schüth, D. Zhao, An aqueous emulsion route to synthesize mesoporous carbon vesicles and their nanocomposites. *Adv. Mater.* 22, 833–837 (2010).
38. C. Liu, X. Huang, J. Wang, H. Song, Y. Yang, Y. Liu, J. Li, L. Wang, C. Yu, Hollow mesoporous carbon nanocubes: Rigid-interface-induced outward contraction of metal-organic frameworks. *Adv. Funct. Mater.* 28, 1705253 (2018).
39. T. Wang, Y. Sun, L. Zhang, K. Li, Y. Yi, S. Song, M. Li, Z. A. Qiao, S. Dai, Space-confined polymerization: Controlled fabrication of nitrogen-doped polymer and carbon microspheres with refined hierarchical architectures. *Adv. Mater.* 31, 1807876 (2019).
40. C. Chen, H. Wang, C. Han, J. Deng, J. Wang, M. Li, M. Tang, H. Jin, Y. Wang, Asymmetric flasklike hollow carbonaceous nanoparticles fabricated by the synergistic interaction between soft template and biomass. *J. Am. Chem. Soc.* 139, 2657–2663 (2017).

41. J. Liu, T. Yang, D. Wang, G. Q. Lu, D. Zhao, S. Z. Qiao, A facile soft-template synthesis of mesoporous polymeric and carbonaceous nanospheres. *Nat. Commun.* **4**, 2798 (2013).

42. D. S. Bin, Z. X. Chi, Y. Li, K. Zhang, X. Yang, Y. G. Sun, J. Y. Piao, A. M. Cao, L. J. Wan, Controlling the compositional chemistry in single nanoparticles for functional hollow carbon nanospheres. *J. Am. Chem. Soc.* **139**, 13492–13498 (2017).

43. M. Hu, A. A. Belik, M. Imura, Y. Yamauchi, Tailored design of multiple nanoarchitectures in metal-cyanide hybrid coordination polymers. *J. Am. Chem. Soc.* **135**, 384–391 (2013).

44. J. Wang, H. Tang, L. Zhang, H. Ren, R. Yu, Q. Jin, J. Qi, D. Mao, M. Yang, Y. Wang, P. Liu, Y. Zhang, Y. Wen, L. Gu, G. Ma, Z. Su, Z. Tang, H. Zhao, D. Wang, Multi-shelled metal oxides prepared via an anion-adsorption mechanism for lithium-ion batteries. *Nat. Energy* **1**, 16050 (2016).

45. J. Wang, J. Wan, D. Wang, Hollow multishelled structures for promising applications: Understanding the structure-performance correlation. *Acc. Chem. Res.* **52**, 2169–2178 (2019).

46. S. Liu, L. Han, Y. Duan, S. Asahina, O. Terasaki, Y. Cao, B. Liu, L. Ma, J. Zhang, S. Che, Synthesis of chiral TiO_2 nanofibre with electron transition-based optical activity. *Nat. Commun.* **3**, 1215 (2012).

47. W. Ma, F. Cheng, Y. Liu, Deep-learning-enabled on-demand design of chiral metamaterials. *ACS Nano* **12**, 6326–6334 (2018).

48. H. Yang, G. A. Ozin, C. T. Kresge, The role of defects in the formation of mesoporous silica fibers, films, and curved shapes. *Adv. Mater.* **10**, 883–887 (1998).

49. Y. Wu, G. Cheng, K. Katsov, S. W. Sides, J. Wang, J. Tang, G. H. Fredrickson, M. Moskovits, G. D. Stucky, Composite mesostructures by nano-confinement. *Nat. Mater.* **3**, 816–822 (2004).

50. S. Che, Z. Liu, T. Ohsuna, K. Sakamoto, O. Terasaki, T. Tatsumi, Synthesis and characterization of chiral mesoporous silica. *Nature* **429**, 281–284 (2004).

51. C. Tan, X. Qi, Z. Liu, F. Zhao, H. Li, X. Huang, L. Shi, B. Zheng, X. Zhang, L. Xie, Z. Tang, W. Huang, H. Zhang, Self-assembled chiral nanofibers from ultrathin low-dimensional nanomaterials. *J. Am. Chem. Soc.* **137**, 1565–1571 (2015).

52. K. Ariga, T. Mori, T. Kitao, T. Uemura, Supramolecular chiral nanoarchitectonics. *Adv. Mater.* **32**, 1905657 (2020).

53. K. S. Sing, Reporting physisorption data for gas/solid systems with special reference to the determination of surface area and porosity (Recommendations 1984). *Pure Appl. Chem.* **57**, 603–619 (1985).

54. E. Peled, S. Menkin, Review—SEI: Past, present and future. *J. Electrochem. Soc.* **164**, A1703–A1719 (2017).

55. W. J. Kim, S. M. Yang, Helical mesostructured tubules from Taylor vortex-assisted surfactant templates. *Adv. Mater.* **13**, 1191–1195 (2001).

56. Z. Lin, S. Liu, W. Mao, H. Tian, N. Wang, N. Zhang, F. Tian, L. Han, X. Feng, Y. Mai, Tunable self-assembly of diblock copolymers into colloidal particles with triply periodic minimal surfaces. *Angew. Chem. Int. Ed.* **129**, 7241–7246 (2017).

57. D. R. Dreyer, D. J. Miller, B. D. Freeman, D. R. Paul, C. W. Bielawski, Elucidating the structure of poly(dopamine). *Langmuir* **28**, 6428–6435 (2012).

58. F. Chen, Y. Xing, Z. Wang, X. Zheng, J. Zhang, K. Cai, Nanoscale polydopamine (PDA) meets π-π interactions: An interface-directed coassembly approach for mesoporous nanoparticles. *Langmuir* **32**, 12119–12128 (2016).

59. W. Jiang, Z.-b. Qu, P. Kumar, D. Vecchio, Y. Wang, Y. Ma, J. H. Bahng, K. Bernardino, W. R. Gomes, F. M. Colombari, A. Lozada-Blanco, M. Veksler, E. Marino, A. Simon, C. Murray, S. R. Muniz, A. F. De Moura, N. A. Kotov, Emergence of complexity in hierarchically organized chiral particles. *Science* **368**, 642–648 (2020).

60. J. Yang, Z. Ju, Y. Jiang, Z. Xing, B. Xi, J. Feng, S. Xiong, Enhanced capacity and rate capability of nitrogen/oxygen dual-doped hard carbon in capacitive potassium-ion storage. *Adv. Mater.* **30**, 1700104 (2018).

61. Z. Tai, Q. Zhang, Y. Liu, H. Liu, S. X. Dou, Activated carbon from the graphite with increased rate capability for the potassium ion battery. *Carbon* **123**, 54–61 (2017).

62. C. Chen, Z. Wang, B. Zhang, L. Miao, J. Cai, L. Peng, Y. Huang, J. Jiang, Y. Huang, L. Zhang, J. Xie, Nitrogen-rich hard carbon as a highly durable anode for high-power potassium-ion batteries. *Energ. Storage Mater.* **8**, 161–168 (2017).

63. K. Share, A. P. Cohn, R. Carter, B. Rogers, C. L. Pint, Role of nitrogen-doped graphene for improved high-capacity potassium ion battery anodes. *ACS Nano* **10**, 9738–9744 (2016).

64. A. Mahmood, S. Li, Z. Ali, H. Tabassum, B. Zhu, Z. Liang, W. Meng, W. Aftab, W. Guo, Y. Zhang, Ultrafast sodium/potassium-ion intercalation into hierarchically porous thin carbon shells. *Adv. Mater.* **31**, 1805430 (2019).

65. W. Wang, J. Zhou, Z. Wang, L. Zhao, P. Li, Y. Yang, C. Yang, H. Huang, S. J. Guo, Short-range order in mesoporous carbon boosts potassium-ion battery performance. *Adv. Energy Mater.* **8**, 1701648 (2018).

66. M. Chen, W. Wang, X. Liang, S. Gong, J. Liu, Q. Wang, S. Guo, H. Yang, Sulfur/oxygen codoped porous hard carbon microspheres for high-performance potassium-ion batteries. *Adv. Energy Mater.* **8**, 1800171 (2018).

67. W. Yang, J. Zhou, S. Wang, W. Zhang, Z. Wang, F. Lv, K. Wang, Q. Sun, S. Guo, Freestanding film made by necklace-like N-doped hollow carbon with hierarchical pores for high-performance potassium-ion storage. *Energ. Environ. Sci.* **12**, 1605–1612 (2019).

68. D.-S. Bin, X.-J. Lin, Y.-G. Sun, Y.-S. Xu, K. Zhang, A.-M. Cao, L.-J. Wan, Engineering hollow carbon architecture for high-performance K-ion battery anode. *J. Am. Chem. Soc.* **140**, 7127–7134 (2018).

69. Y. Xu, C. Zhang, M. Zhou, Q. Fu, C. Zhao, M. Wu, Y. Lei, Highly nitrogen doped carbon nanofibers with superior rate capability and cyclability for potassium ion batteries. *Nat. Commun.* **9**, 1720 (2018).